Assessing Porcine Iris Elasticity and Mechanical Anisotropy with Optical Coherence Elastography

Christian Zevallos-Delgado[1], Taye T. Mekonnen[1], Fernando Zvietcovich[1], Manmohan Singh[1], Salavat R. Aglyamov[2], and Kirill V. Larin[1*]

[1] Department of Biomedical Engineering, University of Houston, 3517 Cullen Blvd., Room 2027, Houston, TX 77204, USA

[2] Department of Mechanical Engineering, University of Houston, Houston, TX 77204, USA

* e-mail: klarin@Central.UH.EDU

Abstract. The relaxation and contraction of the sphincter and dilator muscles of the iris play a critical role in vision, yet little is known about the biomechanical properties of these muscles. This study aimed to determine the elastic properties of the iris as a function of its anatomy and intraocular pressure. A high-resolution phase-sensitive OCE system was employed to detect acoustic radiation force induced propagation of elastic waves in the porcine iris in situ. Experiments were conducted at four different intraocular pressures (5, 10, 20, and 30 mmHg) with mechanical excitation at 1 kHz. We found that there was no significant difference in the wave speed at the different intraocular pressures. The results show that the stiffness of the iris was significantly higher in the semi-azimuthal orientation (mean wave speed of 2.5 m/s) than in the radial orientation (mean wave speed of 1.5 m/s). These measurements provide essential insights into the elastic properties of the iris, and they can be used for the characterization of eye conditions. © 2021 Journal of Biomedical Photonics & Engineering.

1 Introduction

The iris is located between the sclera and the pupil in the eye and is physically protected by the cornea. The movements of the iris (contraction and dilation) are supported by its structure, which is shaped by sphincter (for contraction) and dilator muscles (for dilation). The iris sphincter is in the pupillary circle, controlling accommodation and the amount of light reaching the retina. The exterior surface is divided into two different portions by the collarette. The collarette is the zone where the sphincter and the dilator muscles overlap [1–3]. The iris possesses two layers, the stroma, which contains most of the vascular tissue and is connected to the sphincter and dilator muscles, and the posterior, which is the pigmented layer mainly composed of melanocytes and fibroblasts [4, 5]. The iris can suffer several lesions and can be altered by diseases such as glaucoma, uveitis, cancer, and physical trauma [5–7]. These lesions can cause severe morphological changes to the iris structure and modify its biomechanical properties [8, 9]. The iris structure can also be altered by drugs which can modify the normal miosis and mydriasis of the iris [10]. In addition to abnormal morphological changes, the iris also undergoes natural variations due to its function in the eye (contraction and expansion) [11]. Several studies have shown interest in determining the biomechanical properties of the iris, under different conditions (*in vivo* or *ex vivo*) using animal models [12–14] or human volunteers [11], using different techniques such as Atomic Force Microscopy (AFM) [15], Optical Coherence Tomography (OCT) [9], and Optical Coherence Elastography (OCE) [11, 14, 16]. Although AFM showed a high capacity to determine the stiffness of the iris, it had several limitations. In AFM, the iris was dissected from the eye, limiting the capacity to study diverse areas of the iris and increasing the degradation of this tissue due to its exposure. Also, during the scanning process, the AFM tip adhered to the tissue, reducing the accuracy of indentation measurements [15]. On the other hand, OCE and OCT have the capacity to determine the biomechanical properties of the iris in its natural state inside the eye.

Dynamic OCE has been widely used in several studies to map the shear or Young's modulus of biological tissues. OCE can use several non-contact approaches to generate displacements in tissue, which is an important advantage when characterizing the biomechanical properties of ocular tissues [17–19]. In ophthalmology, OCE has been extensively used since it is based on a widely adopted imaging modality, OCT, which is also non-contact, high-resolution, and highly sensitive to motion [20, 21]. Thus, OCE is rapidly gaining popularity for assessing tissue biomechanical properties [22, 23]. OCE can describe the biomechanical differences among the different tissues of the same organs, such as the detailed description of the biomechanical properties of the inner structure of the eye [20, 24–26], including the iris [11, 16]. However, these studies have not investigated the effects of intraocular pressure (IOP) changes on the stiffness of the iris. These changes of IOP might cause variations in the iris structure and elasticity, which is related to diseases such as glaucoma [27–29]. Also, prior studies have reported the existence of rotational and translational movements of the iris during changes of IOP inside the eye. These movements could cause variations in the biomechanical properties of the iris [9]. To our knowledge, previous OCE methods used to analyze the iris biomechanics did not investigate possible stiffness variations caused by IOP changes [11, 16]. The aim of this work was to demonstrate the elastic properties of the iris using an animal model (porcine eyes) at different IOPs. Here, we demonstrate that the anatomical segments of the iris possess a significant difference in their biomechanical properties, suggesting their different roles during the iris contraction and expansion and their possible function in case of an abnormal deformation.

2 Materials and Methods

2.1 Biological sample preparation

Nine porcine eyes were used in this study (Sioux-Preme Packing Co., Sioux City, IA, USA). All eyes were used during the first 24 h after enucleation. All external tissues (fat and muscles) were manually removed, and whole eye-globes were placed in a custom holder. All samples were analyzed *in situ* using a closed-loop IOP control system simulating conditions of 5, 10, 20, and 30 mmHg of IOP for each sample [30]. To achieve the artificial IOP control, the micro-infusion pump and pressure transducer were connected via tubing, which was then connected to a needle that cannulated the porcine eye-globe. For each eye sample, one additional measurement was conducted before applying the artificial IOPs. Thus, this instance of OCE measurement was undertaken at the intraocular fluid pressure inside the eye-globe. The eyes were constantly hydrated using 1X PBS before and after each OCE imaging session at every IOP condition.

2.2 OCE system setup and measurement

The schematic of the experimental acquisition setup, which is mainly composed of a phase-sensitive spectral domain OCT (SD-OCT) system and an excitation source,

is shown in Fig. 1(a). The SD-OCT system used a superluminescent diode light source (Broadlighter S840-I-B-20, Superlum, Cobh Cross, Ireland) with a ~49 nm bandwidth and ~840 nm of central wavelength. In air, the lateral resolution of the OCT beam was ~8 µm, the axial resolution was ~9 µm, and the axial sampling resolution of the system was ~3 µm/pixel. For this particular study, the A-line acquisition speed was set to 50 kHz (temporal resolution $\Delta t = 20$ µs) [31].
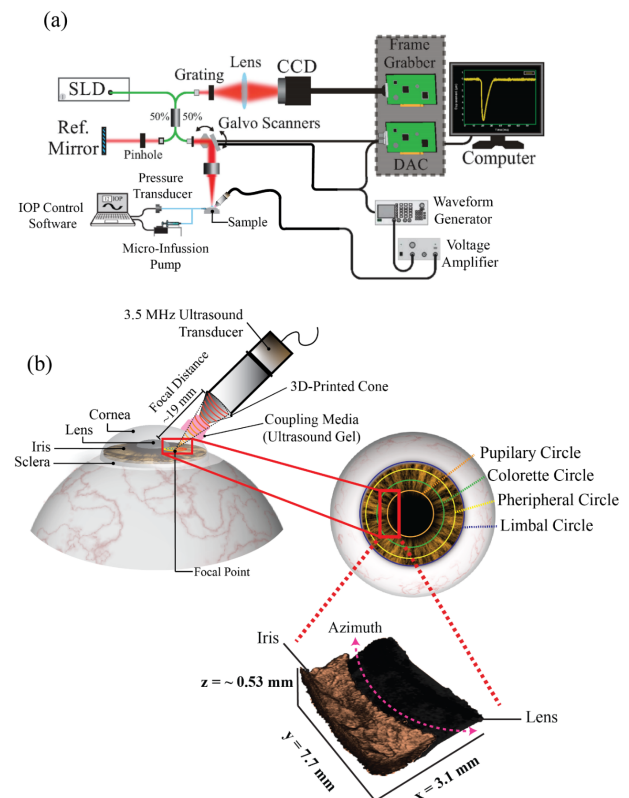

Fig. 1 (a) Schematic representation of the OCE scan setup, including the IOP control and an SD-OCT system. (b) Diagram of the scanned region using the immersion ultrasound transducer (inclined at ~45°) focused on the selected area of the iris.

The Acoustic Radiation Force (ARF) excitation used in this work was generated using an ultrasound immersion transducer with a central frequency of 3.5 MHz and a focal length of ~19 mm (V382-SU, Olympus Corp., Japan) connected to a waveform generator (DG4162, RIGOL Tech, China) and an RF signal amplifier (1040L, Electronics & Innovation Ltd., NY, USA). A custom 3D printed cone was attached to the transducer and filled with ultrasound gel (McKesson Ultrasound Gel Pink, Richmond, VA) to couple the ARF to the eye-globe. The acoustic beam was focused on the iris inside the eye, and the transducer was inclined at an angle of ~45° with respect to the OCT beam. The transducer sent an acoustic pulse that was synchronized with the OCT frame trigger for M-B mode imaging [32–34]. The acoustic excitation pulse was sent in a train

of pulses using a frequency of 1 kHz. The OCT beam was steered with a pair of galvanometer-mounted mirrors for 2D OCE acquisition. The 2D-OCE scanning on the iris was performed in two directions, radial (X-axis) and orthogonal oriented direction with respect to the radial direction (Y-axis). The Y-axis covers a section of the azimuthal orientation of the iris (i.e., near azimuthal), and hence, it will be referred to as semi-azimuthal in this paper (shown in Fig. 1(b)). The ARF-induced elastic waves were tracked during N = 251 A-line repetitions (~5 ms) in a line for Y-axis (7.7 mm) and X-axis (3.1 mm) (Fig. 1(b)). The ARF excitation was focused in the middle of the OCE field of view. Four measurements were performed for each sample at each IOP. The wave speed was quantified from the axial particle velocity, v_z, based on the depth dependent phase (φ) difference of two consecutive complex value A-lines for a given position (x_0, y_0) [35] using the following equation:

$$v_z(z,t) = \Delta\varphi(z,t)\frac{\lambda_0}{4\pi n \Delta t}, \qquad (1)$$

where n was the refractive index of the sample (in this study, the refractive index of the cornea $n = 1.376$ was used) [24, 36], Δt was the temporal resolution, and $\Delta\varphi(z,t) = \varphi(z, t + \Delta t) - \varphi(z,t)$, and λ_0 was the central wavelength of the OCT system. The temporal phase change was used to extract temporal displacement changes ($\Delta d_z(z,t) = \Delta\varphi(z,t)\frac{\lambda_0}{4\pi n}$) along depth, resulting in a spatiotemporal image for each M-B mode OCT image. Subsequently, the elastic wave velocity was determined by computing the slope of the spatiotemporal images of the wave propagation [24]. At the scan area of interest, the presence of aqueous humor on the anterior surface of the iris forms a liquid-tissue interface while the posterior side of the iris rests on the lens (i.e., tissue-tissue interface) [37]. Here, a Scholte wave model is used to describe the elastic wave at the liquid-tissue interface. The velocity of shear wave (C_s) in an incompressible medium is related to the Scholte wave speed (C_{sch}) using the equation [11, 37]:

$$C_{sch} = 0.846\, C_s. \qquad (2)$$

The Young's modulus (E) was estimated using the equation:

$$E = \frac{3\rho}{0.846^2}C_{sch}^2, \qquad (3)$$

where ρ is the density of the iris (~1250 kg/m³). All OCE data sets were analyzed using MATLAB R2020b (Mathworks, Inc., Natick, MA, USA).

The Student's t-test was employed to assess the statistical differences, if any, of the wave propagation speed and the iris stiffness between the semi-azimuthal and the radial directions. A one-way ANOVA was used to determine the significance of differences among the acquisition repetitions and the iris stiffness at the different IOPs. This statistical method was used in all

measurements, and significant difference values are shown in the results section.

3 Results

The wave propagation in the porcine iris was quantified and compared at four artificially induced IOPs (5, 10, 20, and 30 mmHg) and in the eyeball with no intraocular pressure control. Also, we investigated the potential variation in the wave speed for two scan orientations: radial and semi-azimuthal. Figs. 2(a) and 2(f) show the OCT B-mode images, while the instantaneous wave propagation snapshots for the radial and semi-azimuthal scans are shown in Figs. 2(b) to 2(e) and 2(g) to 2(j), respectively, at the noted times after ARF excitation. For comparison purposes, a common excitation position was maintained for all samples and all IOPs for each direction. Fig. 2(a) shows the iris cross-section in the radial orientation where the transition between the dilator and sphincter regions is visible as a large bump near the middle of the OCT structural image. For all samples, two scans were performed in each orientation. In Figs. 2(a) and 2(f), the red arrows indicate the excitation positions. Hence, as shown by the colored patterns, in Figs. 2(b) – 2(e) and 2(g) – 2(j), the wave propagates in both the left and right direction with respect to the excitation position.

Fig. 3 is the box and whisker plots of the mean wave speed at IOPs of 5 mmHg, 10 mmHg, 20 mmHg, and 30 mmHg for all eye samples. In Fig. 3, the 'NAP' (i.e., no artificial intraocular pressure) indicates the additional measurement taken without any artificial IOP. The top and bottom boundaries of the box are the 25th and 75th percentiles, respectively, while the median and mean are shown by the horizontal line and dot inside the box, respectively. The whiskers extend from the 1st and 3rd quartiles to the lowest and largest wave speeds, which are indicated by an 'X'. Statistical testing by a one-way ANOVA showed no significant change in the wave speed as a function of the IOP in the radial ($F(4,48) = 1.00$, $p = 0.42$) or semi-azimuthal directions ($F(4,72) = 0.68$, $p = 0.61$).

As discussed in the methods section, two orthogonal M-B mode scans, one in the radial and the other in the semi-azimuthal orientation, were performed at each repetition. In this study, the semi-azimuthal scan was performed in the orthogonal direction to the radial orientation, and hence, the scan path does not perfectly follow the circumferential direction concentric to the curvature of the iris. But with sufficiently short lateral scan length, the measurements are sufficiently representative of the iris stiffness in the azimuthal direction. Fig. 4 shows the mean and standard deviations of wave speed as a function of IOP for all eye samples. The wave speed in the radial direction was consistently lower than that of the semi-azimuthal direction ($p < 0.001$). The Young's modulus was computed for both the radial and semi-azimuthal wave speed measurements. Table 1 shows the summary of the mean and standard deviations of the wave speed and Young's modulus at the five IOPs.
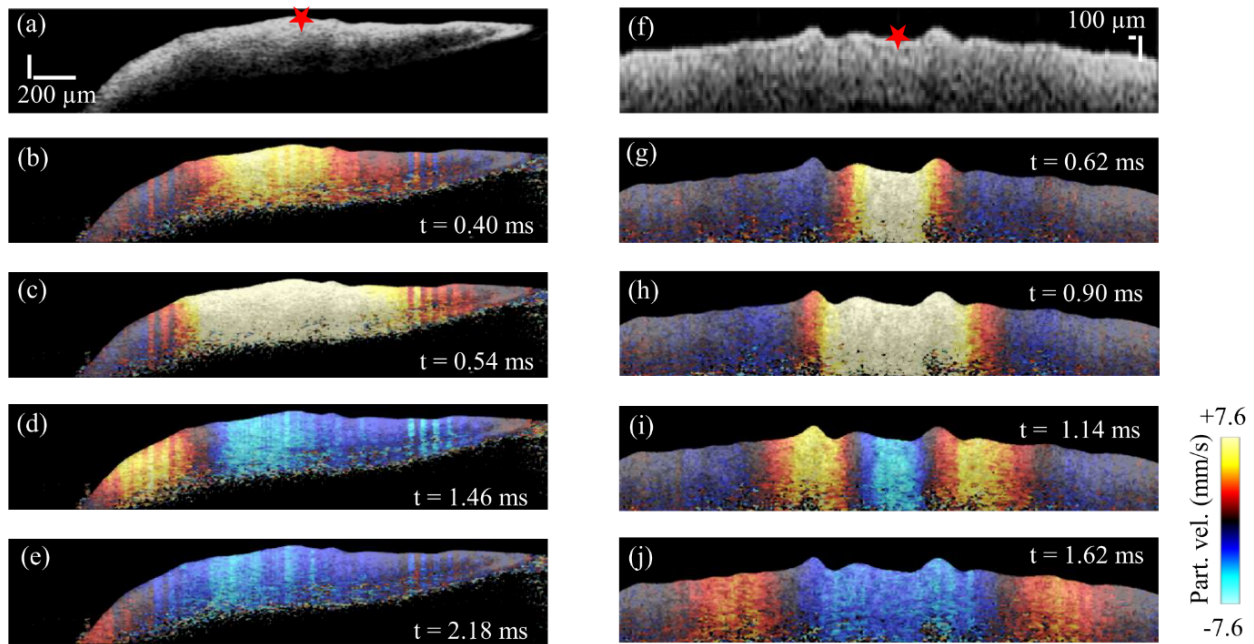
Fig. 2 Representative *ex vivo* OCT structural images of porcine iris scanned in (a) radial and (f) semi-azimuthal directions. The colored images in (b) to (e) and (g) to (j) show particle velocity snapshots extracted at the noted times after 1 kHz ARF excitation in the radial and semi-azimuthal directions, respectively. The excitation points are indicated by the red star in (a) and (f). In the color bar, Part. vel. refers to axial particle velocity in mm/s.

Table 1 Inter-sample mean and standard deviation of Scholte wave speed and Young's modulus at different IOPs (N = 9 samples). SD stands for standard deviation.

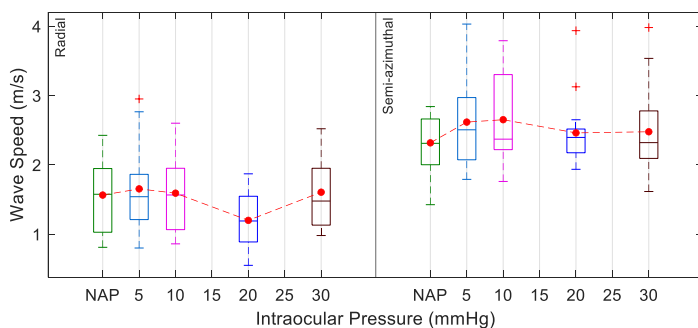| IOP (mmHg) | Radial | | Semi-azimuthal | |
	Elastic wave speed Mean ± SD (m/s)	Young's Modulus Mean ± SD (kPa)	Elastic wave speed Mean ± SD (m/s)	Young's Modulus Mean ± SD (kPa)
NAP	1.56 ± 0.52	14.25 ± 8.65	2.32 ± 0.40	28.95 ± 9.22
5	1.65 ± 0.63	16.42 ± 12.77	2.62 ± 0.63	37.95 ± 18.90
10	1.59 ± 0.56	14.92 ± 10.19	2.65 ± 0.65	39.01 ± 18.72
20	1.20 ± 0.42	8.45 ± 5.59	2.46 ± 0.46	32.81 ± 13.99
30	1.61 ± 0.51	14.87 ± 9.50	2.48 ± 0.61	34.09 ± 17.62
Mean	1.52 ± 0.53	13.78 ± 9.34	2.50 ± 0.55	34.56 ± 15.69

Fig. 3 Box-whisker plot of the mean wave speed for (a) radial and (b) semi-azimuthal OCE measurements in porcine iris at different IOPs. NAP = no artificial intraocular pressure and number of eye samples. N = 9. The red plus ('+') signs indicate outliers in each data set.
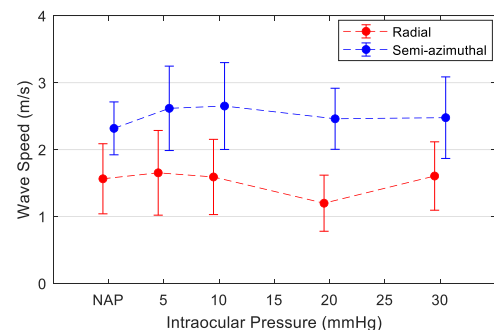
Fig. 4 Mean wave speed comparison between radial and semi-azimuthal orientation. NAP = no artificial intraocular pressure, and the number of eye samples, N = 9.

4 Discussion

One of the main findings of this study was the demonstration that the effect of intraocular pressure on the wave propagation speed in the iris was not significant for either radial or semi-azimuthal directions (Fig. 2).

Despite the similarity in the wave speed trends shown in Fig 3, it appears that the IOP effect on the speed in both the radial and semi-azimuthal orientations is minimal. From this point of view, the iris behavior is similar to the behavior of the crystalline lens under IOP elevation and can be explained by low deformation of these parts of the eye located inside the eye-globe [26, 38–40]. Therefore, hyperplastic properties of the iris and lens do not play a significant role in the wave propagation – in opposite to the cornea and sclera. Lee et al. [9] used OCT imaging to measure the changes in the iris deformation and then quantified iris biomechanical properties with numerical simulations based on the OCT measurements. Their results also showed that there was no consistent trend in the change with iris radial length over different IOPs for murine iris. However, the numerical simulation was produced assuming an isotropic iris and hence, does not reliably reflect the effect of IOP on iris anisotropy as our measurements show a significant degree of elastic anisotropy in the iris.

The current work has shown that the elastic wave speed and hence, the stiffness of the iris is different in the radial and semi-azimuthal orientations. Firstly, the estimated Young's modulus of elasticity in both orientations (Table 1) is comparable to the elasticity of most smooth muscles (i.e. 6 kPa to 2.08 MPa) [41]. Secondly, the higher semi-azimuthal Young's modulus, as compared to the radial Young's modulus, is in agreement with the findings in the previous works [41]. However, to the best of our knowledge, this is the first OCE-based measurement to demonstrate the existence of a significant difference in iris stiffness in the radial and semi-azimuthal orientations. As shown in Fig. 4, the wave speed in the semi-azimuthal orientation is consistently higher. Contrary to the assumptions in some prior studies [11], these results demonstrate the elastic anisotropy of the iris, which is intuitively attributed to the anatomical structure of the dilator and sphincter muscles. The change in the biomechanical properties of these muscles is a common factor for primary angle closure glaucoma [8, 15]. Thus, the accurate quantification of iris elasticity might be used as a potential biomarker of certain eye diseases (e.g., glaucoma) and may help to devise targeted treatment methods. With its high spatial and temporal resolutions and high displacement sensitivity, phase-sensitive OCE promises to be an excellent diagnostic tool for clinical translation to accurately assess the biomechanical properties of the fine muscle fibers of the iris.

In the recent development of OCE-based iris stiffness quantification, Ye et al. [11] employed air-puff for non-contact excitation of elastic waves in the iris. The excitation method avoids the use of an ultrasound gel between the tip of the ARF transducer and the eye-globe. However, unlike the ARF method in which a focused acoustic beam can be directed to the target tissue, the air-puff method does not enable a localized excitation and thus, results in wave motion in various sections of the eye-globe. Moreover, the limited bandwidth afforded by the air puff limits the mechanical resolution and is heavily influenced by the boundary conditions. In earlier OCE-based iris stiffness studies, human [11] and rabbit [16] subjects were used while excised porcine eyeballs were employed for our study, and thus, these might have contributed to the difference in the wave speed results among the three studies.

However, it is important to note the limitations of the current study. Though the semi-azimuthal and radial measurements provided insight into the anisotropic nature of the iris, more accurate elasticity characterization of the dilator and sphincter muscles could be achieved by performing full azimuthal scans in these two regions of the iris. *In situ* studies for various iris colors and different age groups would provide a broader understanding of the iris biomechanical properties. Although a coupling media was utilized in this work, previous work has shown that contact with ocular tissues is well tolerated for brief times even without topical anesthetics [42].

The model of wave propagation used to evaluate Young's modulus in the iris has significant limitations because of the small thickness of the iris (mean thickness of iris in this study was 0.527 mm), and the effect of the contact between the iris and the crystalline lens. While in the model the iris is considered as a homogeneous elastic half-space, such assumption is an obvious simplification and a comprehensive model should include the effects of the lens, anisotropic nature of the iris, viscosity and finite thickness of the iris. Future work will involve the development of an appropriate wave model that incorporates the complex iris biomechanics and geometry.

5 Conclusion

The iris is a fundamental organ in the eye with the crucial role of controlling the amount of light that passes through the lens to the retina. The anatomy of the iris controls the dynamics of contraction and expansion, dominating the biomechanical properties of this tissue structure. In this study, we have shown the changes of the biomechanical properties among the different anatomical parts of the iris, supporting the conclusion that the iris is an anisotropic tissue with different viscoelastic properties in the sphincter, collarette, and dilator muscles. In addition to these changes of the biomechanical properties, the iris is able to keep its shape and properties, even if the ocular globe is under mechanical stress (in this study, the mechanical stress is caused by the internal changes of IOP in the eye). In conclusion, our results suggest that the most significant changes of the biomechanical properties of the iris are related to its anatomical changes caused by natural conditions (contraction and dilation because of variation in the light of the environment) or abnormal modifications (presence of tumors, diseases, or other non-natural modifications). These results suggest the potential use of

OCE to evaluate iris biomechanical properties for disease detection or screening.

Disclosures

All authors declare that there is no conflict of interests in this paper.

References

1. F. Jan, N. Min-Allah, S. Agha, I. Usman, and I. Khan, "A robust iris localization scheme for the iris recognition," Multimedia Tools and Applications, Multimedia Tools and Applications 80(3), 4579–4605 (2021).
2. J. Bloom, M. Motlagh, and C. N. Czyz, "Anatomy, Head and Neck, Eye Iris Sphincter Muscle," In StatPearls, StatPearls Publishing, Treasure Island (2018).
3. K. T. Moazed, The Iris: Understanding the Essentials, Springer Nature, Switzerland (2020). ISBN: 978-3-030-45755-6.
4. L. Di Cecilia, F. Marazzi, and L. Rovati, "A hyperspectral imaging system for the evaluation of the human iris spectral reflectance," Proceedings of SPIE 10045, 100451S (2017).
5. I. Georgalas, P. Petrou, D. Papaconstantinou, D. Brouzas, C. Koutsandrea, and M. Kanakis, "Iris cysts: a comprehensive review on diagnosis and treatment," Survey of Ophthalmology 63(3), 347–364 (2018).
6. W. Xue, S. Lin., X. Chen, Y. Jia, X. Fang, Y. Suo, Y. Ma, Y. Wang, and H. Zou, "In vivo noninvasive imaging and quantitative analysis of iris vessels," Ophthalmic Research 64(5), 754–761 (2021).
7. Z. Da Soh, S. Thakur, S. Majithia, M. E. Nongpiur, and C. Y. Cheng, "Iris and its relevance to angle closure disease: a review," British Journal of Ophthalmology 105(1), 3–8 (2021).
8. J. Hao, H. Fu, Y. Xu, Y. Hu, F. Li, X. Zhang, J. Liu, and Y. Zhao, "Reconstruction and Quantification of 3D Iris Surface for Angle-Closure Glaucoma Detection in Anterior Segment OCT," In International Conference on Medical Image Computing and Computer-Assisted Intervention, Springer, Cham, 704–714 (2020).
9. C. Lee, G. Li, W. D. Stamer, and C. R. Ethier, "In vivo estimation of murine iris stiffness using finite element modeling," Experimental Eye Research 202, 108374 (2021).
10. N. Rashidi, A. D. Pant, S. D. Salinas, M. Shah, V. S.Thomas, Ge Zhang, S.Dorairaj, and R. Amini, "Iris stromal cell nuclei deform to more elongated shapes during pharmacologically-induced miosis and mydriasis," Experimental Eye Research 202, 108373 (2021).
11. S. Ye, Y. Zhou,C. Bao,Y. Chen, F. Lu, and F. Lu, "In vivo non-contact measurement of human iris elasticity by optical coherence elastography," Journal of Biophotonics 14(9), e202100116 (2021).
12. J. E. Whitcomb, R. Amini, N. K. Simha, and V. H. Barocas, "Anterior–posterior asymmetry in iris mechanics measured by indentation," Experimental Eye Research 93(4), 475–481 (2011).
13. Y. Lei, K. Zhang, C. Chen, H. Song, T. Lin, and Z. Liu, "Experimental research on the mechanical properties of porcine iris," Clinical Biomechanics 23, S83–S87 (2008).
14. R. K. Tan, X. Wang, A. S. Y. Chan, M. E. Nongpiur, C. Boote, S. A. Perera, and M. J. A. Girard, "Permeability of the porcine iris stroma," Experimental Eye Research 181, 190–196 (2019).
15. A. Narayanaswamy, M. H. Nai, M. E. Nongpiur, H. M. Htoon, A. Thomas, T. Sangtam, C. T. Lim, T. T. Wong, and T. Aung, "Young's modulus determination of normal and glaucomatous human iris," Investigative Ophthalmology & Visual Science 60(7), 2690–2695 (2019).
16. Y. Zhu, Y. Zhang, G. Shi, Q. Xue, X. Han, S. Ai, J. Shi, C. Xie, and X. He, "Quantification of iris elasticity using acoustic radiation force optical coherence elastography," Applied Optics 59(34), 10739–10745 (2020).
17. M. Singh, A. Nair, S. Aglyamov, and K. V. Larin, "Compressional Optical Coherence Elastography of the Cornea," Photonics 8(4), 111 (2021).
18. V. Y. Zaitsev, A. L. Matveyev, L. A. Matveev, A. A. Sovetsky, M. S. Hepburn, A. Mowla, and B. F. Kennedy, "Strain and elasticity imaging in compression optical coherence elastography: The two-decade perspective and recent advances," Journal of Biophotonics 14(2), e202000257 (2021).
19. V. Y. Zaitsev, A. L. Matveyev, L. A. Matveev, E. V. Gubarkova, A. A. Sovetsky, M. A. Sirotkina, G. V. Gelikonov, E. V. Zagaynova, N. D. Gladkova, and A. Vitkin, "Practical obstacles and their mitigation strategies in compressional optical coherence elastography of biological tissues," Journal of Innovative Optical Health Sciences 10(06), 1742006 (2017).
20. M. A. Kirby, I. Pelivanov, S. Song, L. Ambrozinski, S. J. Yoon, L. Gao, D. Li, T. T. Shen, R. K. Wang, and M. O'Donnell, "Optical coherence elastography in ophthalmology," Journal of Biomedical Optics 22(12), 121720 (2017).
21. V. S. De Stefano, M. R. Ford, I. Seven, and W. J. Dupps Jr., "Live human assessment of depth-dependent corneal displacements with swept-source optical coherence elastography," PLoS One 13(12), e0209480 (2018).

22. B. F. Kennedy, P. Wijesinghe, and D. D. Sampson, "The emergence of optical elastography in biomedicine," Nature Photonics 11(4), 215–221 (2017).
23. K. V. Larin, D. D. Sampson, "Optical coherence elastography–OCT at work in tissue biomechanics," Biomedical Optics Express 8(2), 1172–1202 (2017).
24. F. Zvietcovich, A. Nair, M. Singh, S. R. Aglyamov, M. D. Twa, and K. V. Larin, "Dynamic Optical Coherence Elastography of the Anterior Eye: Understanding the Biomechanics of the Limbus," Investigative Ophthalmology & Visual Science 61(13), 7 (2020).
25. R. Wallace, M. Kirby, L. Gao, S. Song, I. Pelivanov, K. Zhou, R. K. Wang, M. O'Donnell, and T. Shen, "Time-resolved detection of corneal UV Collagen Cross-linking (CXL) using Non-contact Optical Coherence Elastography (OCE)," Investigative Ophthalmology & Visual Science 60(9), 6831–6831 (2019).
26. Y. Li, J. Zhu, J. J. Chen, J. Yu, Z. Jin, Y. Miao, A. W. Browne, Q. Zhou, and Z. Chen, "Simultaneously imaging and quantifying in vivo mechanical properties of crystalline lens and cornea using optical coherence elastography with acoustic radiation force excitation," APL Photonics 4(10), 106104 (2019).
27. S. Jouzdani, R. Amini, and V. H. Barocas, "Contribution of different anatomical and physiologic factors to iris contour and anterior chamber angle changes during pupil dilation: theoretical analysis," Investigative Ophthalmology & Visual Science 54(4), 2977–2984 (2013).
28. H. A. Quigley, "Iris cross-sectional area decreases with pupil dilation and its dynamic behavior is a risk factor in angle closure," Journal of Glaucoma 18(3), 173–179 (2009).
29. F. Aptel, P. Denis, "Optical coherence tomography quantitative analysis of iris volume changes after pharmacologic mydriasis," Ophthalmology 117(1), 3–10 (2010).
30. M. D. Twa, J. Li, S. Vantipalli, M. Singh, S. Aglyamov, S. Emelianov, and K. V. Larin, "Spatial characterization of corneal biomechanical properties with optical coherence elastography after UV cross-linking," Biomedical Optics Express 5(5), 1419–1427 (2014).
31. S. Wang, K. V. Larin, "Noncontact depth-resolved micro-scale optical coherence elastography of the cornea," Biomedical Optics Express 5(11), 3807–3821 (2014).
32. S. Wang, K. V. Larin, "Shear wave imaging optical coherence tomography (SWI-OCT) for ocular tissue biomechanics," Optics Letters 39(1), 41–44 (2014).
33. F. Zvietcovich, M. Singh, Y. S. Ambekar, S. R. Aglyamov, M. D. Twa, and K. V. Larin, "Micro Air-Pulse Spatial Deformation Spreading Characterizes Degree of Anisotropy in Tissues," IEEE Journal of Selected Topics in Quantum Electronics 27(4), 1–10 (2020).
34. J. R. Rippy, M. Singh, S. R. Aglyamov, and K. V. Larin, "Ultrasound Shear Wave Elastography and Transient Optical Coherence Elastography: Side-by-Side Comparison of Repeatability and Accuracy," IEEE Open Journal of Engineering in Medicine and Biology 2, 179–186 (2021).
35. F. Zvietcovich, J. P. Rolland, J. Yao, P. Meemon, and K. J. Parker, "Comparative study of shear wave-based elastography techniques in optical coherence tomography," Journal of Biomedical Optics 22(3), 035010 (2017).
36. K. M. Meek, C. Knupp, "Corneal structure and transparency," Progress in Retinal and Eye Research 49, 1–16 (2015).
37. W. M. Ewing, W. S. Jardetzky, and F. Press, "Elastic waves in layered media," Graw-Hill Book Company, USA (1957).
38. C. Wu, S. R. Aglyamov, H. Zhang, and K. V. Larin, "Measuring the elastic wave velocity in the lens of the eye as a function of intraocular pressure using optical coherent elastography," Quantum Electronics 49(1), 20 (2019).
39. S. Park, H. Yoon, K. V. Larin, S. Y. Emelianov, and S. R. Aglyamov, "The impact of intraocular pressure on elastic wave velocity estimates in the crystalline lens," Physics in Medicine & Biology 62(3), N45 (2017).
40. C. Wu, S. R. Aglyamov, Z. Han, M. Singh, C.-H. Liu, and K. V. Larin, "Assessing the biomechanical properties of the porcine crystalline lens as a function of intraocular pressure with optical coherence elastography," Biomedical Optics Express 9(12), 6455–6466 (2018).
41. J. Heys, V. Barocas, "Mechanical characterization of the bovine iris," Journal of Biomechanics 32(9), 999–1003 (1999).
42. A. M. G. Baptista, R. A. R. C. De Sousa, P. M. Serra, C. M. D. S. Abreu, and C. M. L. R. Da Silva, "Evaluation of discomfort of Goldmann tonometry without anaesthetic," Ophthalmic and Physiological Optics 30(6), 854–859 (2010).